An Integrated Observer for Real-Time Estimation of Vehicle Center of Gravity Height

Giseo Park and Seibum B. Choi, *Member, IEEE*

***Abstract*—This paper introduces a new integrated observer for estimating the vehicle center of gravity (CG) height in real time. It can assist the vehicle in monitoring the real-time rollover risk and improving the performance of vehicle safety control systems. The proposed integrated observer consists of three parts: a linearized recursive least square (LRLS) algorithm on vehicle longitudinal motion, an adaptation law on vehicle lateral motion, and observer synthesis. First, the LRLS algorithm performs estimation of vehicle mass and CG height during longitudinal braking and exploits the characteristic that normalized longitudinal tire stiffness is the same in the front and rear axles. Second, the adaptation law, accompanied by a roll angle observer, estimates CG height on the vehicle lateral motion based on Lyapunov stability analysis. It includes the following contributions: verification of robustness to the vehicle mass estimation error and prevention of integration drift. Finally, in the observer synthesis, the final estimation of CG height combining the above two results is derived. The overall estimation algorithm has high practicality due to the following features. 1) CG height can be obtained on both longitudinal and lateral motions of the vehicle. This point leads to a fast convergence rate in CG height estimation. 2) The fact that it does not cause any computational burden issues in real-time implementation is also a great advantage in terms of practicality. 3) It utilizes only readily available sensors. An experimental study with various driving scenarios evaluates the effectiveness of the proposed algorithm in real-car application.**

***Index Terms*— Center of gravity height, real-time estimation, linearized recursive least square, adaptation law, Lyapunov stability**

I. Introduction

KNOWING precisely the vehicle parameters is greatly helpful in determining the appropriate control intervention timing and control input for various active safety systems ensuring vehicle safety without driver intervention [1]. These systems are considered narrowly as advanced driver assistance systems and broadly as intelligent transportation systems. Among the vehicle parameters, the vehicle center of gravity (CG) height is the information that needs to be monitored in real time in order to maintain the safety of the vehicle behavior [2-4]. Typical applications of vehicle CG height are as follows. 1) It improves the performance of the electronic brake distribution system by contributing to accurate estimation of the vertical tire force of each wheel in braking situations [5]. 2) When designing the anti-lock brake system (ABS) and traction control system (TCS) based on the vehicle longitudinal model, the vehicle CG height information is utilized [6]. 3) This is also used to compute rollover risk, which is the most important reason to accurately estimate the vehicle CG height in real time [4].

There are two types of vehicle rollover: tripped and untripped rollovers [7]. A tripped rollover caused by external inputs accounts for most of single-vehicle rollover accidents [2]. Generally, this occurs when the vehicle is hit by an object such as a curb or a guardrail or enters a steep slope. In contrast, an untripped rollover is due to destabilization of vehicle cornering. According to the Insurance Institute for Highway Safety's (IIHS's) records in 2019, 42 % of sport utility vehicle (SUV) fatalities in 2018 occurred in rollover accidents [8].

It is the rollover index (ROI) that represents the likelihood of occurrence of these vehicle rollovers in real time. This ROI has been already applied to vehicle safety control systems, such as electronic stability control system (ESCs) and roll stability control system (RSCs) [9]. For example, the optimal control intervention timing and control input for RSCs can be determined according to how much ROI exceeds a threshold value. An incorrect ROI may result in the deactivation of RSCs in an emergency when the probability of vehicle rollover is high [10].

Several ROI formulas introduced in existing papers include vehicle CG height information [2-4, 9-11]. Hence, if this information is not accurate, more than tens of percent of ROI error may occur. The nominal value of CG height is given by the vehicle design value, but there is a difference between the nominal and the actual values when a large additional weight is loaded: in particular, when an additional load is placed on the roof of the vehicle, a larger change of the vehicle CG height can occur.

In existing papers, state-of-the-art algorithms for CG height estimation were suggested. They each have advantages in convergence time, estimation accuracy or computation burden.

In [3, 4, 11-16], algorithms based on dynamic modeling of

Manuscript received; revised; accepted. Date of publication; data of current version. This research was partly supported by the National Research Foundation of Korea (NRF) grant funded by the Korea government (MSIP) (No. 2020R1A2B5B01001531); the grant (20TLRP-C152478-02) from Transportation & Logistics Research Program funded by Ministry of Land, Infrastructure and Transport (MOLIT) of Korea government and Korea Agency for Infrastructure Technology Advancement (KAIA); the BK21+ program through the NRF funded by the Ministry of Education of Korea; and the Technology Innovation Program or Industrial Strategic Technology Development Program (10084619, Development of Vehicle Shock Absorber (Damper) and Engine Mount Using MR Fluid with Yield Strength of 60kPa) funded By the Ministry of Trade, Industry & Energy (MOTIE, Korea).

Giseo Park and Seibum B. Choi (Corresponding Author) are with the Department of Mechanical Engineering, Korea Advanced Institute of Science and Technology (KAIST), Daejeon 34141, Korea (e-mail: giseo123@kaist.ac.kr; sbchoi@kaist.ac.kr).

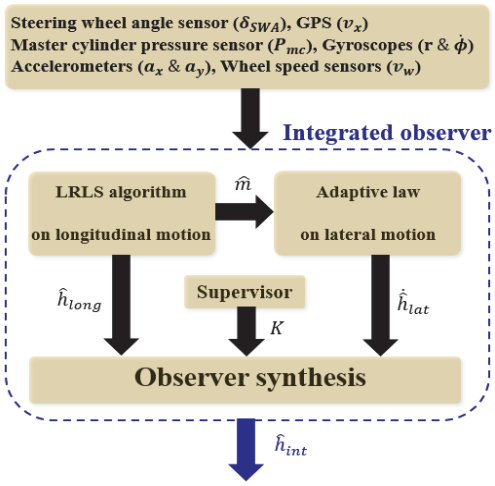

Fig. 1. Algorithm overview.

vehicle lateral motion were introduced. In [3], the authors proposed a method for selecting a model with the smallest error cost function among multiple-models with different CG height values. However, the disadvantage of this method was that it required a large number of models to have increased estimation accuracy. In [4], an adaptive observer to observe the roll angle and CG height was proposed. However, this method did not adequately consider the uncertainty of the vehicle mass. In addition, a linearized recursive least square (LRLS) algorithm for the estimation of CG height was presented in [11, 14], but it required an expensive tilt angle sensor to measure the roll angle. Rath et al. [12] suggested an adaptive sliding-mode observer in the presence of sensor faults, unknown inputs, and uncertainties, but experimental verification was not carried out. Also, CG height estimation methods using extended and unscented Kalman filters were presented in [15] and [13], respectively. These nonlinear Kalman filters may cause heavy the computational burden in real-car application. Lastly, auto-regressive with exogenous input model to estimate the roll dynamics transfer function was proposed in [16], but the sideslip angle used in this model cannot be measured by commercial sensors.

Studies based on dynamic modeling of vehicle longitudinal motion were also presented in [17, 18]. In [17], Huang and Wang suggested a Kalman filter algorithm to estimate both the vehicle CG height and the tire instant effective radius. However, a complicated preliminary work was required to predefine the relationship between the tire effective radius and the vertical tire force. In [18], a combined Kalman filter method deriving an optimal estimation result reflecting vehicle longitudinal dynamics was proposed, but its complex algorithm structure inevitably led to the heavy computational burden.

A new CG height estimation algorithm with high practicality is proposed in this paper. The most notable feature is the development of an integrated observer, which can be activated on both longitudinal and lateral motions of the vehicle. Compared with existing algorithms, this point is a very outstanding advantage in real-car application.

This paper is comprised of seven sections. In Section II, the overview of the vehicle CG height estimation is introduced. Section III presents the LRLS algorithm on longitudinal motion. Also, the adaptation law on lateral motion is introduced in Section IV. Section V deals with the observer synthesis which allows the integrated observer to be active on both longitudinal and lateral motions of the vehicle. To validate the proposed algorithm, experiment results are evaluated in Section VI. Lastly, the conclusion is presented in Section VII.

II. Algorithm Overview

As shown in Fig. 1, the integrated observer consists of two estimation algorithms, each corresponding to the longitudinal and lateral motions of the vehicle. When longitudinal braking motion by a brake input exceeding the threshold value occurs, the LRLS algorithm outputs the estimated CG height $\hat{h}_{long}$ and the estimated vehicle mass $\hat{m}$. Here, utilizing the same values of the normalized longitudinal tire stiffness of the front and rear axles is the biggest difference that distinguishes it from previous studies (refer to Section III –A).

On the other hand, the adaptation law $\dot{\hat{h}}_{lat}$ is derived to estimate the vehicle CG height on lateral motion of the vehicle by steering commands. In Section IV, this newly designed adaptation law including verification of robustness to vehicle mass estimation error $\tilde{m}$ and prevention of integration drift is proposed.

To combine $\dot{\hat{h}}_{lat}$ and $\hat{h}_{long}$, the observer synthesis with the supervisor signal K is presented in Section V. The value of K is normally 0, but when longitudinal braking motion is detected, it changes to 1 and $\hat{h}_{long}$ is quickly reflected in the final estimation of CG height $\hat{h}_{int}$.

It is highly practical to be able to estimate CG height on both longitudinal and lateral motions of the vehicle, considering the real public roads in which many longitudinal and lateral motions appear repeatedly. It makes the proposed algorithm possible to have fast convergence rate and high accuracy in vehicle CG height estimation: but, the proposed estimation algorithm has to be deactivated when braking control systems such as ABS or ESCs are involved or the outage conditions of global positioning system (GPS) are detected (number of satellites less than 4 or horizontal dilution of precision (HDOP) more than 5) [19, 20].

For the implementation of the integrated observer, the easily available sensor signals from the in-vehicle sensors are utilized, such as steering wheel angle δ_{SWA}, master cylinder pressure P_{mc}, wheel speed v_w, yaw and roll rates r and $\dot{\phi}$, and longitudinal and lateral accelerations a_x and a_y [21]. An additional sensor is the standalone GPS in a cost-effective price range (MiniGmouse from AscenKorea, Inc.), which provides the vehicle longitudinal velocity v_x.

To avoid deterioration of the estimation performance on sloped roads, the proposed estimation algorithm is only active when driving on flat roads. When the difference between 2-D and 3-D vehicle speeds measured by GPS is smaller than a certain value, it can be determined that the vehicle is currently driving on flat roads [22].

With regard to the real-time application to mass-produced vehicles [23], the advantages of the proposed estimation

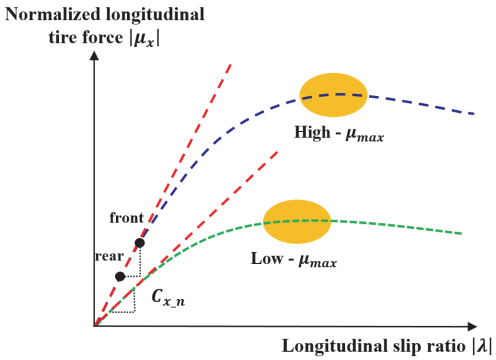

Fig. 2. Normalized longitudinal tire force versus longitudinal slip ratio.

algorithm are summarized as follows: 1) fast convergence rate due to consideration of both longitudinal and lateral motions, 2) no computational burden issues in real-time implementation, 3) robustness verification of vehicle mass estimation error and various driving maneuvers, and 4) use of readily available sensors, such as in-vehicle sensors and additional GPS.

III. LRLS Algorithm on Longitudinal Motion

A. Vertical Tire Forces of Front and Rear Axles

To develop LRLS algorithm, the lumped vertical tire forces of front and rear axles F_{zf} $(= F_{z,fl} + F_{z,fr})$ and F_{zr} $(= F_{z,rl} + F_{z,rr})$ are defined without the vehicle CG height information (in existing studies, the vertical tire forces are obtained using the vehicle CG height). The longitudinal tire force at each wheel during braking is expressed as follows (a minor part, the rolling resistance force, is not taken into account) [24]:

$$F_{x,i} = \left(J_w \dot{v}_{w,i}/R_e + T_{B,i}\right)/R_e \quad i = fl, fr, rl, rr \tag{1}$$

where the braking torque at each wheel is as follows:

$$T_{B,i} = G_{b,i} P_{mc}. \tag{2}$$

Here, J_w is the wheel moment of inertia; R_e the effective tire radius; and G_b the brake gain, respectively. Generally, the brake gain of the front wheel ($G_{bf} = G_{b,fl} = G_{b,fr}$) has a larger value than that of the rear wheel ($G_{br} = G_{b,rl} = G_{b,rr}$) [25]. The lumped longitudinal tire force of each axle is the sum of the left and right forces: $F_{xf} = F_{x,fl} + F_{x,fr}$ and $F_{xr} = F_{x,rl} + F_{x,rr}$.

Figure 2 illustrates the normalized longitudinal tire forces of the front and rear axles $\mu_{xf}\left(= F_{xf}/F_{zf}\right)$ and $\mu_{xr}(= F_{xr}/F_{zr})$ versus the longitudinal slip ratios λ_f and λ_r: on longitudinal braking motion, $\lambda_f = \lambda_{fl} = \lambda_{fr}$ and $\lambda_r = \lambda_{rl} = \lambda_{rr}$. For safety reasons, most commercial vehicles are designed so that $|\lambda_f|$ is larger than $|\lambda_r|$ [26].

Assuming that tires of the same materials are mounted on the front and rear wheels (regardless of tire size), normalized longitudinal tire stiffness $C_{x,n}$ on a homogenous road surface has the same value in both front and rear axles [26, 27]:

$$C_{x,n} = \mu_{xf}/\lambda_f = \mu_{xr}/\lambda_r. \tag{3}$$

As shown in Fig. 2, even if the value of $C_{x,n}$ changes according to the type of road surface (i.e., tire-road friction coefficient μ_{max}), the equation relationship in (3) is satisfied [26]. The longitudinal slip ratios of the front and rear axles

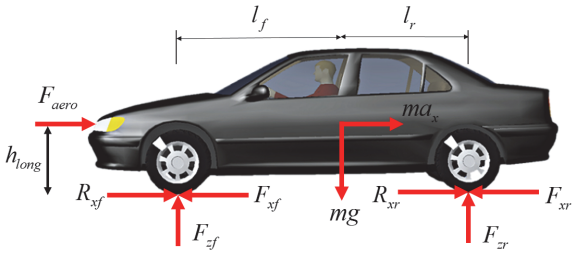

Fig. 3. Vehicle longitudinal dynamics.

during braking are obtained as follows (on longitudinal braking motion, $v_{w,f} = v_{w,fl} = v_{w,fr}$ and $v_{w,r} = v_{w,rl} = v_{w,rr}$).

$$\lambda_f = \left(v_x - v_{w,f}\right)/v_x \tag{4a}$$

$$\lambda_r = \left(v_x - v_{w,r}\right)/v_x \tag{4b}$$

Combining (3) and (4) leads to the following equation.

$$\frac{F_{xf}}{F_{zf}}\frac{v_x}{v_x - v_{w,f}} = \frac{F_{xr}}{F_{zr}}\frac{v_x}{v_x - v_{w,r}} \tag{5}$$

Also, the total vehicle mass m is divided into the nominal m_0 and the additional mass m_{add} (due to additional luggage or passenger boarding). Thus, the expressions for the sum and ratio of F_{zf} and F_{zr} are summarized as follows.

$$F_{zf} + F_{zr} = mg = (m_0 + m_{add})g \tag{6}$$

$$\frac{F_{zf}}{F_{zr}} = \frac{F_{xf}}{F_{xr}}\frac{v_x - v_{w,r}}{v_x - v_{w,f}} \tag{7}$$

Finally, the vertical tire forces of the front and rear axles without the vehicle CG height information are defined as follows.

$$F_{zf} = (m_0 + m_{add})\frac{gF_{xf}(v_x - v_{w,r})}{F_{xf}(v_x - v_{w,r}) + F_{xr}(v_x - v_{w,f})} \tag{8}$$

$$F_{zr} = (m_0 + m_{add})\frac{gF_{xr}(v_x - v_{w,f})}{F_{xf}(v_x - v_{w,r}) + F_{xr}(v_x - v_{w,f})} \tag{9}$$

B. LRLS Algorithm

On the longitudinal braking motion, the estimated value of the vehicle CG height $\hat{h}_{long}$ can be derived. The estimation of $\hat{h}_{long}$ is activated only in the longitudinal braking situation on flat roads without the steering motion (supervisor signal $K = 1$). From the vehicle longitudinal dynamics shown in Fig. 3, the moment balance equation with the origin of the rear tire contact point is as follows (it is assumed that the aerodynamic drag force F_{aero} is applied at the vehicle CG height) [28]:

$$(m_0 + m_{add})(gl_r - h_{long}a_x) - F_{zf}(l_f + l_r) - h_{long}F_{aero} = 0 \tag{10a}$$

where

$$F_{aero} = \rho C_d A_F v_x^2/2. \tag{10b}$$

Here, ρ is the air density; C_d the aerodynamic drag coefficient; and A_F the frontal area of the vehicle. Moreover, l_f and l_r are the CG-front axle and CG-rear axle distances, respectively: it is assumed that l_f and l_r are constant parameters.

The LRLS algorithm is an optimal filter used to estimate unknown parameters [29]. The advantages of LRLS algorithm are as follows [24, 30]. 1) The relatively light computational burden makes it suitable for real-time parameter estimation. 2) It is applicable to nonlinear systems through linearization process. 3) Since its tuning gain is only forgetting factor η, it has a simple and intuitive gain tuning process.

A basic idea of the LRLS algorithm is to find a parameter vector $\boldsymbol{\theta}(t)$ in (11): $n(t)$ denotes the measurement noise.

$$y(t) = f(\boldsymbol{\theta}, t) + n(t) \tag{11}$$

From the vehicle longitudinal dynamics in (10a), the system output $y(t)$, the function of the nonlinear system $f(\boldsymbol{\theta}, t)$, and the parameter vector $\boldsymbol{\theta}(t)$ are given as follows.

$$y(t) = m_0 \frac{gF_{xf}(v_x - v_{w,r})}{F_{xf}(v_x - v_{w,r}) + F_{xr}(v_x - v_{w,f})}\left(l_f + l_r\right) - m_0 g l_r \tag{12}$$

$$f(\boldsymbol{\theta}, t) = m_{add}\left(g l_r - h_{long} a_x\right) - h_{long}(m_0 a_x + F_{aero}) - m_{add} \frac{gF_{xf}(v_x - v_{w,r})}{F_{xf}(v_x - v_{w,r}) + F_{xr}(v_x - v_{w,f})}\left(l_f + l_r\right) \tag{13}$$

$$\boldsymbol{\theta}(t) = [m_{add} \quad h_{long}]^T \tag{14}$$

Under reasonable assumptions that the brake gain and tire radius of all wheels change at similar speeds, respectively, parameter errors of R_e and G_b do not affect the estimation performance of the LRLS algorithm, as well as (12) and (13).

The estimated parameter vector $\widehat{\boldsymbol{\theta}}(t)$ minimizes the cost function $E(\widehat{\boldsymbol{\theta}}, t)$, the sum of the squares of the error between approximated data $f(\widehat{\boldsymbol{\theta}}, t)$ and measured data $y(t)$.

$$E\left(\widehat{\boldsymbol{\theta}}, t\right) = \frac{1}{2}\sum_{i=1}^{t} \eta^{k-i}\left(y(i) - f(\widehat{\boldsymbol{\theta}}, i)\right)^2 \tag{15}$$

The forgetting factor η determines the influence of old samples. As the forgetting factor increases, the influence of older samples on the estimation becomes greater. Generally, the single forgetting factor between 0.9 and 1 is set to be a constant [30]. However, if the parameters, which should be converged at different rates, are all estimated on the LRLS algorithm with the same forgetting factor, the wind-up problem may occur [31]. Thus, the diagonal forgetting matrix $\boldsymbol{\Lambda}$ whose diagonal element η_j is the forgetting factor of $j\,th$ parameter is derived as follows (in this paper, $j = 1, 2$):

$$\boldsymbol{\Lambda} = diag[\eta_1, \eta_2]. \tag{16}$$

The estimated parameter $\hat{h}_{long}$ transmitted to the observer synthesis in Section V should be output smoothly without noise. Therefore, it is recommended that the forgetting factor corresponding to $\hat{h}_{long}$ be larger than that of $\hat{m}_{add}$: $\eta_1 = 0.995$ for $\hat{m}_{add}$ and $\eta_2 = 0.999$ for $\hat{h}_{long}$ in this paper. By differentiating $E(\widehat{\boldsymbol{\theta}}, t)$ with respect to $\widehat{\boldsymbol{\theta}}(t)$, the forms of LRLS algorithm with the diagonal forgetting matrix $\boldsymbol{\Lambda}$ can be derived as follows.

$$\widehat{\boldsymbol{\theta}}(t) = \widehat{\boldsymbol{\theta}}(t-1) + \boldsymbol{L_{LRLS}}(t)\left(y(t) - f(\widehat{\boldsymbol{\theta}}(t-1), t)\right) \tag{17}$$

$$\boldsymbol{L_{LRLS}}(t) = (\boldsymbol{\Lambda} + \boldsymbol{F^T}(t)\boldsymbol{P}(t-1)\boldsymbol{F}(t)\boldsymbol{I_{2\times 2}})^{-1}\,\boldsymbol{P}(t-1)\boldsymbol{F}(t) \tag{18}$$

$$\boldsymbol{P}(t) = \boldsymbol{\Lambda^{-1}}\left(\boldsymbol{I_{2\times 2}} - \boldsymbol{L_{LRLS}}(t)\boldsymbol{F^T}(t)\right)\boldsymbol{P}(t-1) \tag{19}$$

Here, $\boldsymbol{L_{LRLS}}(t)$ and $\boldsymbol{P}(t)$ are the update gain and the error covariance matrix, respectively. Also, the Jacobian matrix $\boldsymbol{F^T}(t)$ is as follows.

$$\boldsymbol{F^T}(t) = \left.\frac{\partial f(\boldsymbol{\theta}, t)}{\partial \boldsymbol{\theta}}\right|_{\boldsymbol{\theta}=\widehat{\boldsymbol{\theta}}(t-1)} \tag{20}$$

$$= \left[\begin{matrix} g l_r - h_{long} a_x - \dfrac{gF_{xf}\left(v_x - v_{w,r}\right)\left(l_f + l_r\right)}{F_{xf}\left(v_x - v_{w,r}\right) + F_{xr}\left(v_x - v_{w,f}\right)} \\ -m_{add} a_x - m_0 a_x - F_{aero} \end{matrix}\right]^T \Bigg|_{\boldsymbol{\theta}=\widehat{\boldsymbol{\theta}}(t-1)}$$

Actually, the relationship (3) is inaccurate in the high-slip region. Therefore, the LRLS algorithm is deactivated and the value of the estimated $\widehat{\boldsymbol{\theta}}(t)$ is held in the high-slip region ($\left|\lambda_f\right| \geq \lambda_{th}$). Deactivation of the LRLS algorithm is also done in split-μ conditions when the differences between left and right wheel speeds increase significantly ($\left|v_{w,fl} - v_{w,fr}\right|, \left|v_{w,rl} - v_{w,rr}\right| \geq v_{w,th}$).

Also, to cope with the changes of longitudinal CG locations l_f and l_r, the real-time estimation algorithm of longitudinal CG location introduced in [32] can be utilized.

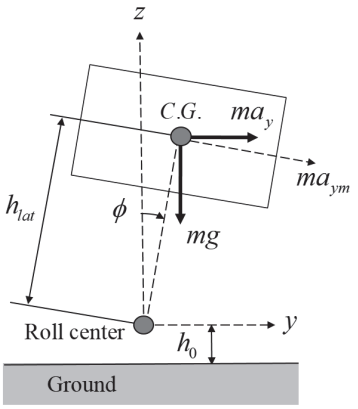

Fig. 4. Roll dynamics.

IV. Adaptation Law on Lateral Motion

A. Roll Angle Observer

Figure 4 shows the y-z cross-section of the vehicle, and the centrifugal force ma_y and gravity mg are both expressed at the vehicle CG. In this figure, the actual lateral acceleration at the vehicle CG is a_y, and the lateral acceleration measured from the accelerometer is a_{ym}. The roll moment arm h_{lat} denotes the distance between the vehicle CG and the roll center.

The force ma_{ym} from the vehicle lateral motion causes the roll dynamics of the vehicle. The roll center height h_0 from the ground changes depending on the driving situation, but this change is sufficiently small to be negligible so that h_0 is assumed to be a constant. Therefore, the estimation of the roll moment arm h_{lat} implies the estimation of the vehicle CG height h on lateral motion: $h = h_0 + h_{lat}$.

The design of the adaptation law to estimate h_{lat} begins with the design of a roll angle observer. The roll dynamics equation at the vehicle CG is as follows:

$$I_x\ddot{\phi} = (\hat{m} + \tilde{m})a_{ym}h_{lat} - k_t\phi - c_t\dot{\phi} \tag{21}$$

Here, $\hat{m}(= m_0 + \hat{m}_{add})$ is from the LRLS algorithm in Section III and $\tilde{m}(= m - \hat{m})$ the vehicle mass estimation error; I_x the vehicle roll moment of inertia; k_t the vehicle roll stiffness coefficient; c_t the vehicle roll damping coefficient; and ϕ the vehicle roll angle, respectively.

Next, the roll angle observer based on the Luenberger observer scheme is designed as follows.

$$I_x\ddot{\hat{\phi}} = \hat{m}a_{ym}\hat{h}_{lat} - k_t\hat{\phi} - c_t\dot{\hat{\phi}} + L_a\left(\dot{\phi} - \dot{\hat{\phi}}\right) \tag{22}$$

where the roll angle error and the roll moment arm error are as follows:

$$\tilde{\phi} = \phi - \hat{\phi} \tag{23}$$

$$\tilde{h}_{lat} = h_{lat} - \hat{h}_{lat} \tag{24}$$

Here, L_a is the positive Luenberger observer gain. From the difference between (21) and (22), the error dynamics equation can be derived as

$$I_x\ddot{\tilde{\phi}} = \hat{m}a_{ym}\tilde{h}_{lat} + \tilde{m}a_{ym}h_{lat} - k_t\tilde{\phi} - c_t\dot{\tilde{\phi}} - L_a\dot{\tilde{\phi}}. \quad (25)$$

B. Adaptation Law Design

To check the stability of the roll angle observer, a Lyapunov function candidate is derived as follows:

$$V(\boldsymbol{x},t) = \frac{1}{2}\left(\dot{\tilde{\phi}} + \gamma_a\tilde{\phi}\right)^2 + \frac{1}{2k_a}\tilde{h}_{lat}^2 \quad (26)$$

where

$$\boldsymbol{x} = \begin{bmatrix}\dot{\tilde{\phi}} + \gamma_a\tilde{\phi} & \tilde{h}_{lat}\end{bmatrix}^T.$$

Here, both k_a and γ_a are the positive adaptation gains. The time derivative of (26) is given by (27).

$$\dot{V}(\boldsymbol{x},t) = \left(\dot{\tilde{\phi}} + \gamma_a\tilde{\phi}\right)\left(\ddot{\tilde{\phi}} + \gamma_a\dot{\tilde{\phi}}\right) - \frac{1}{k_a}\tilde{h}_{lat}\dot{\hat{h}}_{lat} \quad (27)$$

Substituting (25) into (27) yields (28a).

$$\dot{V}(\boldsymbol{x},t) = \left(\dot{\tilde{\phi}} + \gamma_a\tilde{\phi}\right)\left(-\frac{c_t+L_a-I_x\gamma_a}{I_x}\dot{\tilde{\phi}} - \frac{k_t}{I_x}\tilde{\phi}\right) + \tilde{h}_{lat}\left(\frac{\hat{m}a_{ym}}{I_x}\left(\dot{\tilde{\phi}} + \gamma_a\tilde{\phi}\right) - \frac{1}{k_a}\dot{\hat{h}}_{lat}\right) + \frac{\tilde{m}a_{ym}}{I_x}h_{lat}\left(\dot{\tilde{\phi}} + \gamma_a\tilde{\phi}\right) \quad (28a)$$

This is rewritten as (28b).

$$\dot{V}(\boldsymbol{x},t) = -\frac{c_t+L_a-I_x\gamma_a}{I_x}\left(\dot{\tilde{\phi}} + \gamma_a\tilde{\phi}\right)\left(\dot{\tilde{\phi}} + \frac{k_t}{c_t+L_a-I_x\gamma_a}\tilde{\phi}\right) + \tilde{h}_{lat}\left(\frac{\hat{m}a_{ym}}{I_x}\left(\dot{\tilde{\phi}} + \gamma_a\tilde{\phi}\right) - \frac{1}{k_a}\dot{\hat{h}}_{lat}\right) + \frac{\tilde{m}a_{ym}}{I_x}h_{lat}\left(\dot{\tilde{\phi}} + \gamma_a\tilde{\phi}\right) \quad (28b)$$

In order for γ_a to be equal to $k_t/(c_t + L_a - I_x\gamma_a)$, γ_a is set as

$$\gamma_a = \frac{c_t+L_a+\sqrt{(c_t+L_a)^2-4I_xk_t}}{2I_x}. \quad (29)$$

Accordingly, $\dot{V}(\boldsymbol{x},t)$ can be summarized below.

$$\dot{V}(\boldsymbol{x},t) = -\frac{k_t}{I_x\gamma_a}\left(\dot{\tilde{\phi}} + \gamma_a\tilde{\phi}\right)^2 + \tilde{h}_{lat}\left(\frac{\hat{m}a_{ym}}{I_x}\left(\dot{\tilde{\phi}} + \gamma_a\tilde{\phi}\right) - \frac{1}{k_a}\dot{\hat{h}}_{lat}\right) + \frac{\tilde{m}a_{ym}}{I_x}h_{lat}\left(\dot{\tilde{\phi}} + \gamma_a\tilde{\phi}\right) \quad (30)$$

Here, the adaptation law $\dot{\hat{h}}_{lat}$ is designed as follows.

$$\dot{\hat{h}}_{lat} = \frac{k_a\hat{m}a_{ym}}{I_x}\left(\dot{\tilde{\phi}} + \gamma_a\tilde{\phi}\right) \quad (31)$$

Lastly, (31) is assigned to $\dot{\hat{h}}_{lat}$ in (30).

$$\dot{V}(\boldsymbol{x},t) = -\frac{k_t}{I_x\gamma_a}\left(\dot{\tilde{\phi}} + \gamma_a\tilde{\phi}\right)^2 + \frac{\tilde{m}a_{ym}}{I_x}h_{lat}\left(\dot{\tilde{\phi}} + \gamma_a\tilde{\phi}\right) \quad (32)$$

Under the condition that $\tilde{m}$ satisfies

$$|\tilde{m}| \le \frac{k_t}{\gamma_a h_{lat}}\left|\frac{\dot{\tilde{\phi}}+\gamma_a\tilde{\phi}}{a_{ym}}\right|, \quad (33)$$

$\dot{V}(\boldsymbol{x},t) \le 0$ for all $t \ge t_0$. Therefore, the equilibrium point ($\boldsymbol{x_e} = [0 \quad 0]^T$) of V is Lyapunov stable [33]. It implies that if $\|\boldsymbol{x}(t_0) - \boldsymbol{x_e}\| < \zeta$, $\|\boldsymbol{x}(t) - \boldsymbol{x_e}\| < \varepsilon$ for $t \ge t_0$. Here, ζ and ε are positive constant values. Then, $\tilde{\phi}$ and $\tilde{h}_{lat}$ can be bounded with robustness to vehicle mass estimation error $\tilde{m}$. If the vehicle mass is correctly estimated from the LRLS algorithm and $\tilde{m}$ is 0, the adaptation law satisfies the asymptotic stability that both $\tilde{\phi}$ and $\tilde{h}_{lat}$ converge to 0.

From the experimental verification of parameter errors of k_t and c_t, for a CG height estimation error within 10 %, errors of k_t and c_t have to be within about 10 % and 20 %, respectively. Fortunately, both k_t and c_t are parameters that vary relatively slowly, so parameter updates by the operator at long intervals can maintain the performance of the adaptation law. Finally, the roll angle observer (22) with the adaptation law (31) simultaneously yields the estimated values of the roll angle $\hat{\phi}$ and the vehicle CG height $h_0 + \hat{h}_{lat}$.

C. Prevention of Integration Drift

Considering the roll angle error $\tilde{\phi}$ (=$\int\dot{\phi}\,dt - \int\dot{\hat{\phi}}\,dt$) in (31), the integral of the measured roll rate $\int\dot{\phi}\,dt$ can be drifted to an incorrect value due to the sensor offset of the gyroscope. Accordingly, $\hat{h}_{lat}(=\int\dot{\hat{h}}_{lat}\,dt)$ in (31) can be also drifted. A method to prevent this integration drift is designed as follows. First, the relationship between a_y and a_{ym} is utilized [34]:

$$a_{ym} = a_y cos\phi + gsin\phi \approx a_y + g\phi \quad (34)$$

where

$$a_y = \dot{v}_y + rv_x. \quad (35)$$

Here, r and v_y are the vehicle yaw rate and lateral velocity, respectively. In steady states, $\dot{v}_y$ is 0 so that

$$a_{y,ss} = rv_x. \quad (36)$$

Then, the roll angle in steady states can be obtained as

$$\phi_{ss} = (a_{ym} - a_{y,ss})/g = (a_{ym} - rv_x)/g. \quad (37)$$

The condition for detecting the steady state situation is $|\dot{\phi}| \le \dot{\phi}_{th}$ where $\dot{\phi}_{th}$ is the small constant threshold [35]. Lastly, $\int\dot{\phi}\,dt$ is replaced by ϕ_{ss} (free to the integration drift) at each steady state situation.

$$\tilde{\phi} = \begin{cases}\phi_{ss} - \int\dot{\hat{\phi}}\,dt & If\ |\dot{\phi}| \le \dot{\phi}_{th} \\ \int\dot{\phi}\,dt - \int\dot{\hat{\phi}}\,dt & Otherwise\end{cases} \quad (38)$$

As drifted $\tilde{\phi}$ is corrected under steady state situations, the drifted integral of $\hat{h}_{lat}(=\int\dot{\hat{h}}_{lat}\,dt)$ can be also eliminated. The time required to completely eliminate the drifted integral of $\hat{h}_{lat}$ depends on the adaptation gain k_a and the driver steering command. The larger k_a or the more extreme the steering command, the shorter this time.

V. Observer Synthesis

As mentioned above, the estimation output of the LRLS algorithm $\hat{h}_{long}$ in (14) and the adaptation law $\dot{\hat{h}}_{lat}$ in (31) and are combined to derive the final estimation of CG height $\hat{h}_{int}$. The default value of the supervisor signal K is 0. When the pressure of the brake master cylinder exceeds the threshold $P_{mc,th}$ and the lateral motion is not detected, K is switched to 1.

$$K = \begin{cases}1 & (P_{mc} \ge P_{mc,th}, |\delta_{SWA}| \le \delta_{SWA,th}, and\ |\dot{\delta}_{SWA}| \le \dot{\delta}_{SWA,th}) \\ 0 & Otherwise\end{cases} \quad (39)$$

Finally, the integrated observer having the structure of the low-pass filter (LPF) is designed as follows.

$$\dot{\hat{h}}_{int} = (1-K)\dot{\hat{h}}_{lat} + KL_{int}\left(\hat{h}_{long} - \hat{h}_{int}\right) \quad (40)$$

Through the frequency domain analysis, the cut-off frequency L_{int} ($= 2\pi f_{int}$) is determined to remove high-frequency noises of sensor signals: f_{int} is set to 5 Hz in consideration of the trade-off relationship between convergence rate and low-pass filtering. Even if K suddenly changes between 0 and 1, the integrated observer outputs a smoothly changing signal $\hat{h}_{int}$.

When the variance of $\hat{h}_{int}$ over a moving window becomes smaller than a certain threshold, it can be determined that $\hat{h}_{int}$ converges to a stable value.

VI. Experimental Study

To verify the performance of the proposed algorithm for vehicle CG height estimation, Kia Soul, a sport utility vehicle with a high CG height, was used as an experimental vehicle, as shown in Fig. 5 (a). Assuming that the additional luggage of 145 kg was carried on the roof directly above the vehicle CG, l_f and l_r are the same as before loading. Except for I_x and h (before loading, 869.3 kg $\cdot$ m^2 and 563 m, respectively), the other vehicle specifications are the values before loading, as shown in Table I.

The direct current (DC) offsets of accelerometers (a_x and a_y) and gyroscopes (r and $\dot{\phi}$) are -0.1 m/s^2, -0.07 m/s^2, 0.003 rad/s, and 0.004 rad/s, respectively. To compensate for these DC offsets, the sensor offset estimator introduced in [21] is utilized. The RT-3002 from Oxford Technical Solutions is a high-precision measurement system, so that the roll angle measured by the RT-3002 is regarded as the actual value. This device was located close to the vehicle CG (see Fig. 5 (b)). Also, GPS receiver was mounted on the vehicle roof to measure the vehicle longitudinal velocity [36]. The sampling times of in-vehicle sensors and GPS are 10 ms and 100 ms, respectively. Through the observer-based filtering, the raw signal of the vehicle longitudinal velocity from GPS is converted into the filtered signal with a sampling time of 10 ms. The estimation algorithm built into the Micro-Autobox runs with a sampling time of 10 ms on the controller area network. Figure 5 (c) shows photographs of the driving test course.

During the driving tests, GPS measurement is accurate due to an open-sky environment. From simple to complex driving tests in Section VI, the estimation performance of the proposed algorithm for various driving maneuvers can be confirmed. The following constant gain values were applied in experimental tests: $L_a = 12000$, $\gamma_a = 20.39$, and $k_a = 0.015$.

A. Braking Tests (Verification of LRLS Algorithm $\hat{h}_{long}$)

To verify the performance of LRLS algorithm, longitudinal braking tests were performed on two types of road surface. Figures 6 and 7 show the results of the longitudinal braking tests on dry asphalt and basalt surfaces, respectively (the value of each tire-road friction coefficient μ_{max} is 0.9 and 0.45).

On the flat dry asphalt surface, the vehicle brakes with a constant longitudinal acceleration of -0.6 g at an initial longitudinal velocity of 80 km/h, as shown in Fig. 6 (a). The longitudinal tire forces of the front and rear axles F_{xf} and F_{xr} can be seen in Fig. 6 (b), which are derived from (1).

During 7 to 9.7 s, the vehicle runs at a constant longitudinal velocity of 80 km/h, so both F_{xf} and F_{xr} are near 0. After 9.7 s, they begin to change rapidly with the driver's braking command. Since the brake gain of the front axle is larger than that of the rear axle, the magnitude of F_{xf} becomes larger than the magnitude of F_{xr}.

TABLE I
Vehicle Specifications

Parameter	Quantity	Value
m_0	Mass of vehicle and driver (nominal)	1610 kg
m_{add}	Mass of additional luggage	145 kg
l_f	CG-front axle distance	1104 mm
l_r	CG-rear axle distance	1469 mm
I_x	Roll moment of inertia	1008 $kg \cdot m^2$
R_e	Effective tire radius	322 mm
J_w	Wheel moment of inertia	0.7 $kg \cdot m^2$
h	Vehicle CG height (actual)	637 mm
h_0	Roll center height	85.72 mm
k_t	Roll stiffness coefficient	1950 Nm/deg
c_t	Roll damping coefficient	245 $Nm \cdot s/deg$

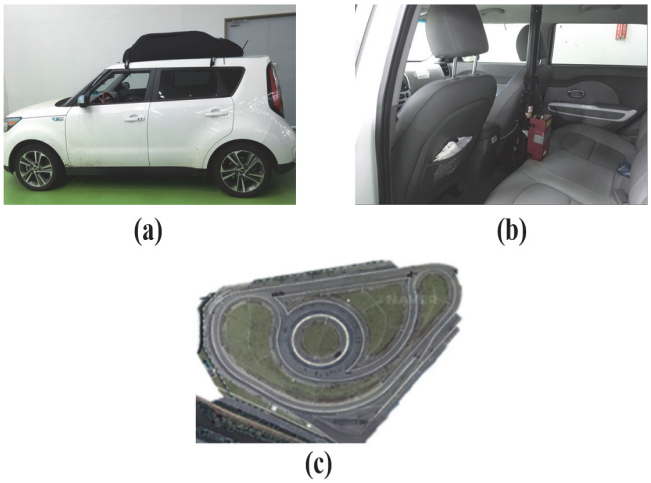

Fig. 5. Experimental environment. (a) Experimental vehicle with additional luggage. (b) Installation of RT-3002 for algorithm verification. (c) Driving test course.

In Fig. 6 (c), both actual and estimated values of the vehicle mass are shown. During 7 to 9.7 s when the master cylinder pressure P_{mc} is not detected, the LRLS algorithm is not activated, so that $\hat{m}$ are held at the initial value m_0. At around 12 s, $\hat{m}$ is estimated to be quite close to the actual value m.

Next, Fig. 6 (d) presents both the reference and the estimated values of the vertical tire forces of the front and rear axles. Here, the reference values including the vehicle CG height information are defined as follows [28].

$$F_{zf,ref} = (mgl_r - mha_x - hF_{aero})/(l_f + l_r) \quad (41)$$

$$F_{zr,ref} = (mgl_f + mha_x + hF_{aero})/(l_f + l_r) \quad (42)$$

Then, estimated values $\hat{F}_{zf}$ and $\hat{F}_{zr}$ are from (8) and (9) including the estimated $\hat{m}_{add}$: their initial values are $mgl_r/(l_f + l_r)$ and $mgl_f/(l_f + l_r)$, respectively. They start to change from 9.7 s when the LRLS algorithm starts to be activated. As $\hat{m}$ in Fig. 6 (c) decreases, $\hat{F}_{zf}$ and $\hat{F}_{zr}$ in Fig. 6 (d) are also accurately estimated. As shown in Fig. 6 (e), after 10 s, values of front and rear axles (i.e. $\mu_{xf}/\lambda_f = (F_{xf}/F_{zf})/\lambda_f$ and $\mu_{xr}/\lambda_r = (F_{xr}/F_{zr})/\lambda_r$) are around 15 on the dry asphalt. Thus, it is verified experimentally that the normalized longitudinal tire stiffness $C_{x,n}$ is the same in both the front and rear axles.

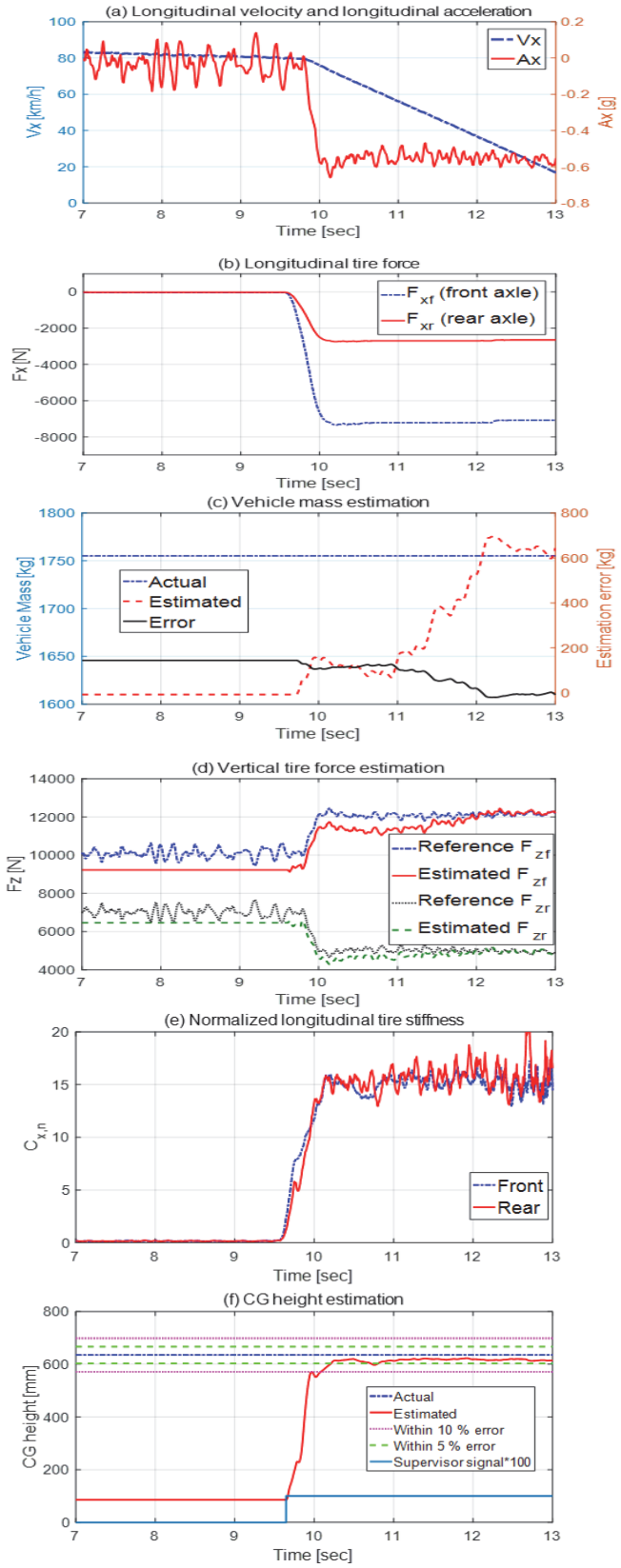

Fig. 6. Braking test on a dry asphalt surface with $\mu_{max} = 0.9$. (a) Longitudinal velocity and longitudinal acceleration. (b) Longitudinal tire force. (c) Vehicle mass estimation. (d) Vertical tire force estimation. (e) Normalized longitudinal tire stiffness. (f) CG height estimation.

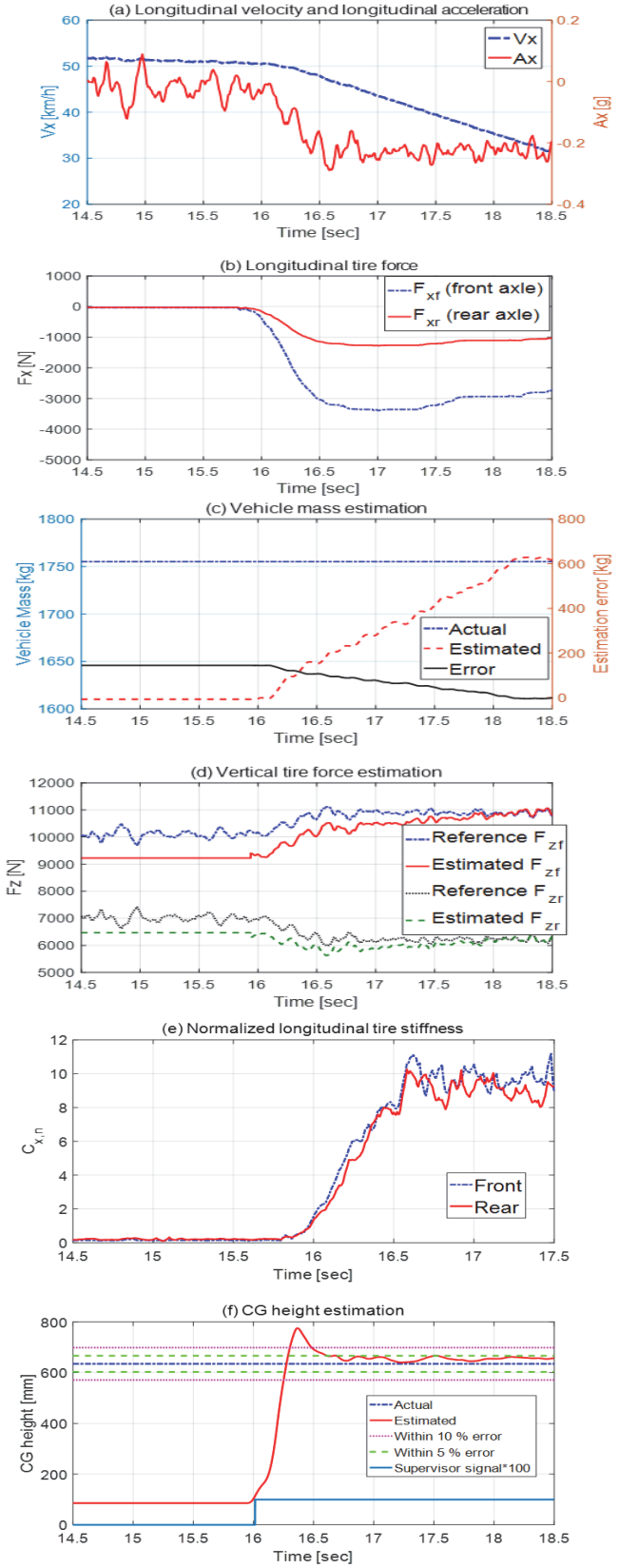

Fig. 7. Braking test on a basalt surface with $\mu_{max} = 0.45$. (a) Longitudinal velocity and longitudinal acceleration. (b) Longitudinal tire force. (c) Vehicle mass estimation. (d) Vertical tire force estimation. (e) Normalized longitudinal tire stiffness. (f) CG height estimation.

TABLE II
BRAKING TEST RESULTS WITH CHANGES OF LONGITUDINAL CG LOCATIONS

Case	Change of l_f [mm]	Change of l_r [mm]	Estimation error of CG height [mm]
1	0	0	-18
	(0 %)	(0 %)	(-2.82 %)
2	33	-33	28
	(3 %)	(-2.25 %)	(4.39 %)
3	-33	33	-36
	(-3 %)	(2.25 %)	(-5.65 %)
4	55	-55	85
	(5 %)	(-3.75 %)	(13.3 %)
5	-55	55	-91
	(-5 %)	(3.75 %)	(-14.3 %)

( ): rate of change.

Because of the longitudinal braking situation, the supervisor signal K represents 1 in this test. Thus, $\hat{h}_{long}$ from the LRLS algorithm on the dry asphalt surface is shown in Fig. 6 (f). Here, to confirm the convergence rate of CG height estimation effectively, the initial value of $\hat{h}_{long}$ is the roll center height h_0. The most noticeable point in Fig. 6 (f) is the highly fast convergence rate of the estimated CG height $\hat{h}_{long}$.

To perform the longitudinal braking test on the flat basalt surface, the initial v_x and the constant a_x were set to 50 km/h and -0.25 g, respectively (see Fig. 7 (a)). As shown in Fig. 7 (b), magnitudes of longitudinal tire forces are smaller than those in Fig. 6 (b). Even on different road surfaces, the estimation accuracy of the vehicle mass and vertical tire force is still very high, as shown in Figs. 7 (c) and (d).

In Fig. 7 (e), the normalized longitudinal tire stiffness $C_{x,n}$ is estimated at a value of about 9.5, which is smaller than that in Fig. 6 (e). The result in Fig. 7 (f) shows that although the overshoot of the estimated value exists, it is confirmed that the estimation error finally converges to within 5 %. Therefore, it is verified in these braking tests that the LRLS algorithm on longitudinal motion achieves CG height estimation with fast and accurate convergence regardless of the road surface type.

As the distribution of luggage on the vehicle roof changes, both l_f and l_r change (at this time, the actual vehicle CG height is not changed). To verify the robustness to the changes of l_f and l_r, braking tests (same as the test in Fig. 6) were performed on vehicles with different longitudinal CG positions. The proposed algorithm with $l_f = 1104\ mm$ and $l_r = 1469\ mm$ was run in each test and the estimation results are shown in Table II. From these estimation results, it is confirmed that the changes of l_f and l_r have to be within about 3 % for a CG height estimation error within 5 %.

B. Steering Tests (Verification of Adaptation Law $\dot{\hat{h}}_{lat}$)

Steering tests were conducted to verify the estimation performance when the adaptation law on lateral motion was utilized alone. On the flat dry asphalt surface with $\mu_{max} = 0.9$, circle turn and slalom steering tests were performed, respectively. Since the LRLS algorithm is not activated throughout these tests, the estimated $\hat{m}_{add}$ is 0 and the estimation error of the vehicle mass $\tilde{m}$ is m_{add} (=145 kg).

As shown in Fig. 8 (a), the vehicle follows a circular track with a radius of 35 m, increasing the longitudinal velocity from 0 to 50 km / h. The lateral acceleration is up to 0.75 g. To

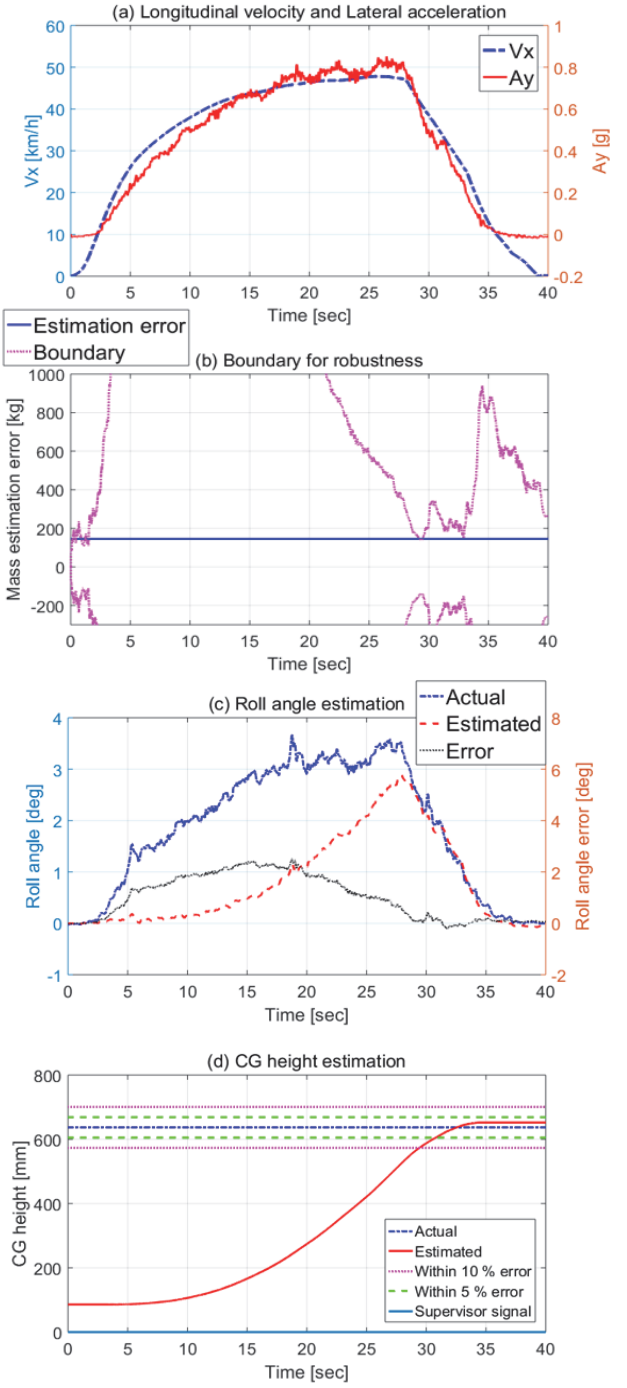

Fig. 8. Circle turn test on a dry asphalt surface with $\mu_{max} = 0.9$. (a) Longitudinal velocity and lateral acceleration. (b) Vehicle mass estimation error and boundary for robustness of the adaptation law. (c) Roll angle estimation. (d) CG height estimation.

guarantee the robustness to the vehicle mass estimation error $\tilde{m}$, the satisfaction of Lyapunov stability of the adaptation law is checked in Fig. 8 (b). The boundary $\left(k_t\left|\dot{\tilde{\phi}} + \gamma_a\tilde{\phi}\right|\right) / \left(\gamma_a h_{lat}|a_{ym}|\right)$ in (33) has a minimum magnitude at about 28 s when the maximum lateral acceleration occurs, and $\tilde{m}$ of 145 kg exists within the boundary. Therefore, throughout this circle turn test, the inequality condition (33) is satisfied so that the equilibrium point $(\boldsymbol{x_e} = [0 \quad 0]^T)$ is Lyapunov stable. It

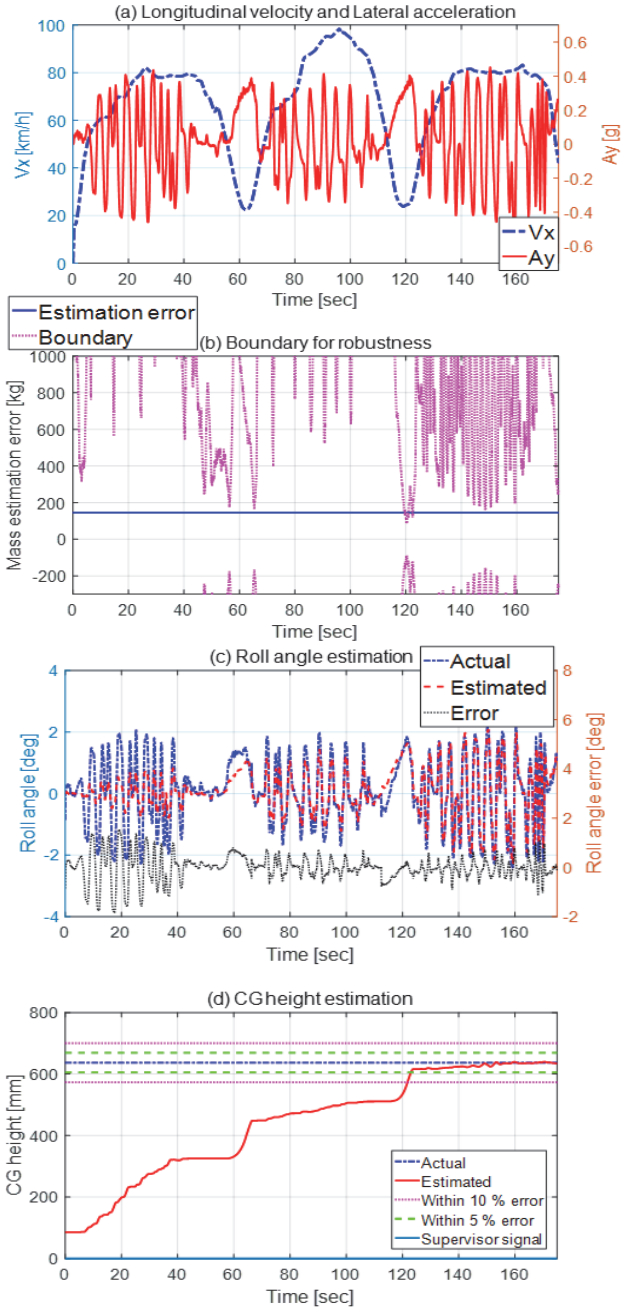

Fig. 9. Slalom steering test on a dry asphalt surface with $\mu_{max} = 0.9$. (a) Longitudinal velocity and lateral acceleration. (b) Vehicle mass estimation error and boundary for robustness of the adaptation law. (c) Roll angle estimation. (d) CG height estimation.

guarantees that $\boldsymbol{x} = [\tilde{\phi} \quad \tilde{h}_{lat}]^T$ is bounded within a positive constant ε even though the vehicle mass estimation error $\tilde{m}$ exists throughout this circle turn test.

Figure 8 (c) shows the difference between the actual and estimated values of the vehicle roll angle. As CG height estimation becomes more accurate over time, the estimation accuracy of the roll angle also becomes higher.

Lastly, Fig. 8 (d) shows the estimated CG height $h_0 + \hat{h}_{lat}$ from the adaptation law. The initial value is the roll center height h_0. Since the longitudinal braking situation in which the supervisor signal K becomes 1 does not occur in this test, K continues to be 0.

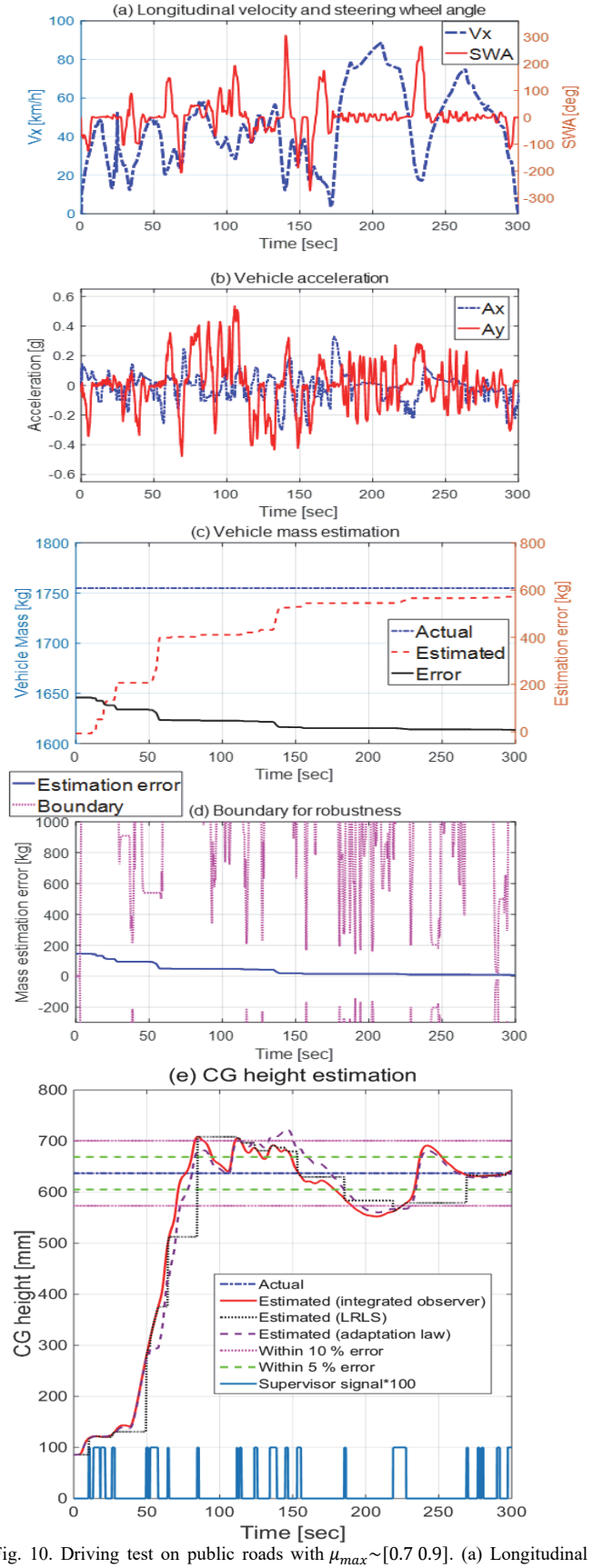

Fig. 10. Driving test on public roads with μ_{max}~[0.7 0.9]. (a) Longitudinal velocity and steering wheel angle. (b) Vehicle acceleration. (c) Vehicle mass estimation. (d) Vehicle mass estimation error and boundary for robustness of the adaptation law. (e) CG height estimation.

The estimation accuracy is also quite low at the beginning of Fig. 8 (d) when $h_0 + \hat{h}_{lat}$ is far from the actual CG height h. CG height estimation error of less than 5 % is recorded at around 30 s, and thereafter, the estimated value continues to be generated close to the actual value. If the adaptation gain γ_a is changed, the convergence time to reach the actual value can be adjusted.

Next, the slalom steering test within a lateral acceleration range of -0.45 g to 0.45 g was conducted, which included three slalom steering maneuvers. Between these maneuvers, two U-turn maneuvers with the steady states of roll dynamics were conducted to reverse the direction of the vehicle.

Figure 9 (a) shows a profile of vehicle longitudinal velocity that starts at an initial 20 km/h and increases to a maximum of 100 km/h. During the U-turn maneuver, the driver stepped on the brake pedal to reduce the vehicle longitudinal velocity.

As can be seen from the vigorously varying lateral acceleration in Fig. 9 (a), the slalom steering maneuver leads to extreme lateral motion. It is the purpose of this maneuver to verify that the adaptation law is properly implemented even in such extreme cornering.

For most of this test, $\tilde{m}$ of 145 kg exists within the boundary so that the inequality condition (33) is satisfied, as shown in Fig. 9 (b). However, $\tilde{m}$ exceeds the boundary in some intervals. Since these are relatively short intervals for the total test time, they have little impact on the overall Lyapunov stability of the adaptation law in this test. If the LRLS algorithm is accompanied to reduce $\tilde{m}$, (33) is expected to be satisfied throughout this slalom steering test. Similar to the previous circle turn test, the estimation error of the roll angle in Fig. 9 (c) decreases gradually over time in this slalom steering test.

It can be seen in Fig. 9 (d) that the estimated CG height converges to the actual value h at different rates in both slalom steering and U-turn maneuvers. After 120 s, it is confirmed that the estimation error continues to be maintained within 5 %.

C. Driving Test on Public Roads (Verification of Integrated Observer $\hat{h}_{int}$)

The final test was for CG height estimation on public roads to verify the estimation performance of the integrated observer. The driving course is flat on average and consists of the asphalt road of μ_{max} distributed in the range between approximately 0.7 and 0.9. As shown in Fig. 10 (a), the longitudinal velocity of the vehicle varies in a wide range from 0 to 90 km/h for a relatively long period of time, approximately 5 minutes. Because there are several driving sections that require vehicle cornering, the steering command in Fig. 10 (a) is generated.

As can be seen in Fig. 10 (b), longitudinal acceleration and deceleration situations occur repeatedly. The respective ranges of the longitudinal and lateral accelerations during this driving test are as follows: a_x~[-0.3 g 0.3 g] and a_y~[-0.5 g 0.5 g]. Figures 10 (a) and (b) show that this driving test properly reflects the normal driving maneuvers of many drivers on public roads.

Whenever the LRLS algorithm is activated, the estimated vehicle mass $\hat{m}$ increases to converge to the actual value m, as shown in Fig. 10 (c). After 230 s, the vehicle mass estimation error is close to 0. As shown in Fig. 10 (d), since $\tilde{m}$ exists within the boundary (i.e. the inequality condition (33) is satisfied), it is verified that the Lyapunov stability of the adaptation law is satisfied throughout this driving test.

Lastly, CG height estimation result $\hat{h}_{int}$ from the integrated observer can be seen in Fig. 10 (e). Also, $\hat{h}_{lat}$ (from the adaptation law) and $\hat{h}_{long}$ (from the LRLS algorithm) are shown, which are activated when the supervisor signal K is 0 and 1, respectively. Because driving on public roads is difficult to give driving commands that achieve an estimate quickly as in Sections VI-A and B, the convergence rates in Fig. 10 (e) are inevitably slower than those in Sections VI-A and B.

Actually, the public roads in this driving test are not perfectly flat. Especially on gently sloped roads, since the difference between 2-D and 3-D vehicle speeds measured by GPS may be quite small, it is practically difficult to detect some slop sections quickly and accurately. Thus, around 200 s in Fig. 10 (e), the deterioration of estimation accuracy is because the vehicle travels on these undetectable slope sections.

However, after that, the estimated $\hat{h}_{int}$ quickly converges to the actual value with an estimation error within 5%. In actual driving environment, even if the estimation accuracy is dropped by the undetectable slope sections, it is expected to recover quickly on the flat roads.

VII. Conclusion

This paper proposed a novel integrated observer for real-time estimation of the vehicle CG height. The goal of the algorithm is to activate the estimation on both longitudinal and lateral motions of the vehicle. This is an advantage that makes it possible to improve the convergence rate of the vehicle CG height estimation. The integrated observer smoothly combines the two estimation outputs from the adaptation law on lateral motion and the LRLS algorithm on longitudinal braking motion. Through experiments with various driving scenarios, it is confirmed that the proposed algorithm shows satisfactory convergence rate and accuracy in the vehicle CG height estimation. The main contributions of this study distinguished from the existing studies are summarized as follows.

1) LRLS algorithm on longitudinal braking motion is a new method for the estimation of both vehicle mass and CG height using the equality of normalized longitudinal tire stiffness values of the front and rear axles. It can be used on any kind of road surface.

2) In the design process of the adaptation law on lateral motion, a method to prevent the integration drift is proposed. Also, the boundary for robustness to the vehicle mass estimation error is newly designed to satisfy the Lyapunov stability of the adaptation law.

3) With the exception of some deactivation conditions (GPS outage, implementation of braking control systems, sloped roads, and nonhomogenous road surfaces), the proposed algorithm is easily applicable to the actual driving environment of mass-produced vehicles. Also, with simple and intuitive structure, no computational burden issues are found in real-time implementation.

In conclusion, this research demonstrates that the proposed estimation algorithm with high practicality can be a meaningful solution to monitor the vehicle CG height in real time. Therefore, it is expected to contribute to improving the driving safety of commercial vehicles.

REFERENCES

[1] D. Piyabongkarn, R. Rajamani, J. A. Grogg, and J. Y. Lew, "Development and Experimental Evaluation of a Slip Angle Estimator for Vehicle Stability Control," *IEEE Trans. Cont. Sys. Technol.*, vol. 17, no. 1, pp. 78-87, 2009.

[2] G. Phanomchoeng and R. Rajamani, "New Rollover Index for the Detection of Tripped and Untripped Rollovers," *IEEE Trans. Ind., Elec*., vol. 60, no. 10, pp. 4726-4736, 2013.

[3] S. Solmaz, M. Akar, R. Shorten, and J. Kalkkuhl, "Real-time multiple-model estimation of centre of gravity position in automotive vehicles," *Vehi. Sys. Dyn*., vol. 46, no. 9, pp. 763-788, 2008.

[4] S. B. Choi, "Practical vehicle rollover avoidance control using energy method," *Vehi. Sys. Dyn*., vol. 46, no. 4, pp. 323-337, 2008.

[5] D. Kim and H. Kim, "Vehicle Stability Control with Regenerative Braking and Electronic Brake Force Distribution for a Four-Wheel Drive Hybrid Electric Vehicle," *Proc. Inst. Mech. Eng. D, J. Autom. Eng.,* vol. 220, no. 6, pp. 683-693, 2006.

[6] K. Cho, J. Kim, and S. B. Choi, "The integrated vehicle longitudinal control system for ABS and TCS," in *Proc. IEEE Int. Conf. Cont. Applic.,* Dubrovnik, Croatia, 2012.

[7] "Types of rollovers," NHTSA, Washington, DC, Aug 24, 2012. [Online]. Available: http://www.safercar.gov.

[8] "Fatality Facts 2018 Passenger vehicle occupants," IIHS, Arlington, VA, 2019. [Online]. Available: https://www.iihs.org/topics/fatality-statistics.

[9] J. Yoon and K. Yi, "A rollover mitigation control scheme based on rollover index," in *Proc. Amer. Control Conf.,* Minneapolis, MN, 2006.

[10] J. Yoon, W. Cho, B. Koo, and K. Yi, "Unified Chassis Control for Rollover Prevention and Lateral Stability," *IEEE Trans. Veh. Technol*., vol. 58, no. 2, pp. 596-609, 2009.

[11] R. Rajamani, D. Piyabongkarn, V. Tsourapas, and J. Y. Lew, "Parameter and State Estimation in Vehicle Roll Dynamics," *IEEE Trans. Intell. Transport. Syst*., vol. 12, no. 4, pp. 1558-1567, 2011.

[12] J. J. Rath, M. Defoort, and K. C. Veluvolu, "Rollover Index Estimation in the Presence of Sensor Faults, Unknown Inputs, and Uncertainties," *IEEE Trans. Intell. Transport. Syst.*, vol. 17, no. 10, pp. 2949-2959, 2016.

[13] Z. Deng, D. Chu, F. Tian, Y. He, C. Wu, Z. Hu, and X. Pei, "Online estimation for vehicle center of gravity height based on unscented Kalman filter," in *Proc. Int. Conf. Transport. Inf. Saf.*, Banff, Canada, 2017.

[14] R. Rajamani, D. Piyabongkarn, V. Tsourapas, and J. Y. Lew, "Real-time estimation of roll angle and CG height for active rollover prevention applications," in *Proc. Amer. Control Conf.*, St. Louis, MO, USA, 2009.

[15] J. Huang and W. C. Lin, "EKF-Based In-Vehicle Estimation of Relative CG Height," in *Proc. Dyn. Sys. Con. Conf.*, Ann Arbor, MI, USA, 2008.

[16] F. Momiyama, K. Kitazawa, K. Miyazaki, H. Soma, and T. Takahashi, "Gravity center height estimation for the rollover compensation system of commercial vehicles," *JSAE Review*, vol. 20, no. 4, pp. 493-497, 1999.

[17] X. Hunag and J. Wang, "Center of gravity height real-time estimation for light weight vehicles using tire instant effective radius," *Control Engineering Practice,* vol. 21, pp. 370-380, 2013.

[18] X. Huang and J. Wang, "Real-Time Estimation of Center of Gravity Position for Lightweight Vehicles Using Combined AKF–EKF Method," *IEEE Trans. Veh. Technol*., vol. 63, no. 9, pp. 4221-4231, 2014.

[19] G. Park, Y. Hwang, and S. B. Choi, "Vehicle positioning based on velocity and heading angle observer using low-cost sensor fusion," *ASME J. Dyn. Syst., Meas., Control*, vol. 139, no. 12, pp. 1-13, 2017.

[20] K. Jo, K. Chu, and M. Sunwoo, "Interacting Multiple Model Filter-Based Sensor Fusion of GPS With In-Vehicle Sensors for Real-Time Vehicle Positioning," *IEEE Trans. Intell. Transport. Syst.*, vol. 13, no. 1, pp. 329-343, 2012.

[21] G. Park, S. Choi, D. Hyun, and J. Lee, "Integrated Observer Approach Using In-vehicle Sensors and GPS for Vehicle State Estimation," *Mechatronics*, vol. 50, pp. 134-147, 2018.

[22] K. Jo, M. Lee, and M. Sunwoo, "Road Slope Aided Vehicle Position Estimation System Based on Sensor Fusion of GPS and Automotive Onboard Sensors," *IEEE Trans. Intell. Transport. Syst.*, vol. 17, no. 1, pp. 250-263, 2016.

[23] D. Savitski, B. Shyrokau, and V. Ivanov, "Base-brake functions of electric vehicle: disturbance compensation in decoupled brake system", *Int. J. of Vehicle Design*, vol. 70, no. 1, pp. 69–97, 2016.

[24] M. Choi and S. Choi, "Linearized Recursive Least Square Methods for Real-time Identification of Tire-Road Friction Coefficient," *IEEE Trans. Veh. Technol*., vol. 62, no. 8, pp. 2906-2918, 2013.

[25] K. Han, S. B. Choi, J. Lee, D. Hyun, and J. Lee, " Accurate Brake Torque Estimation With Adaptive Uncertainty Compensation Using a Brake Force Distribution Characteristic," *IEEE Trans. Veh. Technol*., vol. 66, no. 12, pp. 10830-10840, 2017.

[26] K. Han, E. Lee, M. Choi, and S. Choi, "Adaptive Scheme for the Real-Time Estimation of Tire-Road Friction Coefficient and Vehicle Velocity," *IEEE Trans. Mechatronics*, vol. 22, no. 4, pp. 1508-1518, 2017.

[27] H. Pacejka, *Tire and vehicle dynamics.* Elsevier, 2005.

[28] R. Rajamani, *Vehicle Dynamics and control*, New York, NY, USA: Springer-Verlag, 2006.

[29] D. Simon, *Optimal State Estimation*: Wiley New York, 2006.

[30] P. A. Ioannou and J. Sun, Robust adaptive control: Courier Corporation, 2012.

[31] A. Vahidi, A. Stefanopoulou, and H. Peng, "Recursive least squares with forgetting for online estimation of vehicle mass and road grad: Theory and experiments," *Vehi. Sys. Dyn*., vol. 43, no. 1, pp. 31-55, 2005.

[32] J. Lee, D. Hyun, K. Han, and S. Choi, "Real-Time Longitudinal Location Estimation of Vehicle Center of Gravity," *Int. J. Auto. Technol.*, vol. 19, no. 4, pp. 651-658, 2018.

[33] H. K. Khalil and J. Grizzle, *Nonlinear systems* vol. 3: Prentice hall New Jersey, 1996.

[34] S. You, J. Hahn, and H. Lee, "New adaptive approaches to real-time estimation of vehicle sideslip angle," *Control Engineering Practice,* vol. 17, pp. 1367-1379, 2009.

[35] T. A. Wenzel, K. J. Burnham, M. V. Blundell, and R. A. Williams, "Dual extended Kalman filter for vehicle state and parameter estimation," *Vehi. Sys. Dyn*., vol. 44, no. 2, pp. 153-171, 2006.

[36] H. S. Bae, J. Ryu, and J. C. Gerdes, "Road grade and vehicle parameter estimation for longitudinal control using GPS," in *Proc. IEEE Intell. Trans. Syst. Conf.,* pp. 166-171, 2001.

Giseo Park received the B.S. degree in mechanical engineering from Hanyang University, Seoul, Korea, in 2014 and the M.S. and ph.D. degrees in mechanical engineering from Korea Advanced Institute of Science and Technology (KAIST), Daejeon, Korea in 2016 and 2020. His research interests include vehicle dynamics, control theory, active safety systems, autonomous driving system, and optimization.

Seibum B. Choi (M'09) received the B.S. degree in mechanical engineering from Seoul National University, Seoul, Korea; the M.S. degree in mechanical engineering from Korea Advanced Institute of Science and Technology (KAIST), Daejeon, Korea; and the Ph.D. degree in controls from the University of California, Berkeley, CA, USA, in 1993. Since 2006, he has been with the faculty of the Department of Mechanical Engineering, KAIST. His research interests include fuel-saving technology, vehicle dynamics and control, and active safety systems.